IOP PUBLISHING JOURNAL OF PHYSICS: CONDENSED MATTER

J. Phys.: Condens. Matter **20** (2008) 115101 (11pp) doi:10.1088/0953-8984/20/11/115101

Colloid–polymer mixtures in the presence of quenched disorder: a theoretical and computer simulation study

Giuseppe Pellicane[1], Richard L C Vink[2,3], Carlo Caccamo[1] and Hartmut Löwen[2]

[1] Dipartimento di Fisica Contrada Papardo, Università degli Studi di Messina, 98166 Messina, Italy

[2] Institut für Theoretische Physik II: Weiche Materie, Heinrich-Heine-Universität Düsseldorf, Universitätsstraße 1, 40225 Düsseldorf, Germany

Received 22 September 2007, in final form 12 December 2007
Published 20 February 2008
Online at stacks.iop.org/JPhysCM/20/115101

Abstract

We use theory and computer simulation to study the structure and phase behavior of colloid–polymer mixtures in the presence of quenched disorder. The Asakura–Oosawa model (AO) (Asakura and Oosawa 1954 *J. Chem. Phys.* **22** 1255) is used to describe the colloid–colloid, colloid–polymer, and polymer–polymer pair interactions. We then investigate the behavior of this model in the presence of frozen-in (quenched) obstacles. The obstacles will be placed according to two different scenarios, both of which are experimentally feasible. In the first scenario, polymers are distributed at positions drawn from an ideal gas configuration. In the second scenario, colloidal particles are distributed at positions drawn from an equilibrium hard sphere configuration. We investigate how the unmixing transition of the AO model is affected by the type of quenched disorder. The theoretical formalism is based on the replica method of Given and Stell (1994 *Physica* A **209** 495). Our foremost aim is to test the accuracy of three common closures to the replica Ornstein–Zernike equations, namely the hypernetted chain, the Percus–Yevick, and the Martinov–Sarkisov equations. The accuracy is determined by comparison with grand canonical Monte Carlo simulations. We find that, for quenched polymer disorder, all three closures perform remarkably well. However, when quenched colloid disorder is considered, i.e. the second mentioned scenario, the predictions of all three closures worsen dramatically.

1. Introduction

The behavior of fluid phases in the presence of quenched disorder has received considerable attention over the years. In part, this is due to the strong link to technological applications [1]. However, there is also a link to fundamental physics, since quenched disorder in fluids gives rise to 'random-fields' [2]. Consequently, these systems have received considerable attention in experiments [3, 4], and sparked numerous theoretical and simulational investigations [5–15]. On the theoretical side, the study of fluids with quenched disorder has had a boost, thanks to the concept of the 'quenched–annealed' mixture, proposed by Madden and Glandt [5]. Here, a fluid of mobile particles is confined to a random matrix of immobile particles, with the structure of the random matrix drawn from some equilibrium high-temperature distribution. In a subsequent paper, Madden generalized this approach to the case where the structure of the random matrix was essentially arbitrary [6]. In both cases, the corresponding Ornstein–Zernike relations describing the structure of this quenched–annealed system were derived. In 1994, Given and Stell demonstrated that these relations were in fact approximate, and formulated a new set of formally exact equations, called the *replica* Ornstein–Zernike (ROZ) equations [7]. Recently, Paschinger and Kahl [15] generalized the ROZ equations to the case of a two-component fluid with quenched disorder, i.e. a fluid of two mobile species A and B, confined to a random matrix of species C.

[3] Present address: Institute of Theoretical Physics, Georg-August-Universität, Friedrich-Hund-Platz 1, 37077 Göttingen, Germany.

As for the bulk Ornstein–Zernike equations, numerical solutions of the ROZ equations require that a closure relation be specified. For bulk fluids (by bulk we mean in the absence of quenched disorder), numerous closure relations have been proposed, and their accuracy has been tested quite extensively over the years [16]. In contrast, for fluids with quenched disorder, the accuracy of many closure relations is still untested. The aim of this paper is to improve on this state of affairs. More specifically, we will use the ROZ equations to describe a mixture of colloids and polymers with quenched disorder. The interactions in the mixture are those of the Asakura–Oosawa (AO) model [17, 18]; quenched disorder is introduced according to two scenarios. In the first scenario, polymers are distributed at positions drawn from an ideal gas configuration. In the second scenario, colloids are distributed at positions drawn from an equilibrium hard sphere configuration. For both scenarios, we solve the corresponding ROZ equations using three closure relations, namely (1) the hypernetted chain (HNC) approximation, (2) the Percus–Yevick (PY) equations, and (3) the Martinov–Sarkisov (MS) equations. The predictions of the closures are then compared to grand canonical Monte Carlo (MC) simulations. We present and compare binodal data, as well as pair correlation functions obtained at various state points in the phase diagram. An interesting twist of this investigation is that both the theory and the simulation treat colloid and polymer degrees of freedom explicitly. This means that full information regarding the correlations is available, including those involving the polymer coordinates.

Our main finding is that the integral equation closures can reasonably well predict the structural properties of the AO model in the presence of quenched *polymer* disorder. At low colloid density, HNC performs surprisingly well, but it fails at higher densities. At high colloid density, structural properties are better captured by the PY and MS closures. Regarding the binodal, we found that HNC becomes numerically unstable, but results could still be obtained using PY and MS. In contrast, when quenched *colloid* disorder is considered, the predictions of all three closures worsen dramatically, to the point where qualitative discrepancies with the simulations arise. Our work thus emphasizes the pressing need for improved liquid state theories to predict all the trends correctly.

The outline of this paper is as follows. In section 2 we introduce the AO model, as well as the two types of quenched disorder that we plan to investigate. Next, in section 3, we formulate and solve the ROZ equations for our problem. The simulation method is described in section 4. Our results are presented in section 5, and we end with a discussion and summary in section 6.

2. Model parameters

2.1. The AO model

In the AO model [17, 18], colloids (species c) and polymers (species p) are treated as spheres with respective diameters σ_c and σ_p. Hard sphere interactions are assumed between colloid–colloid and colloid–polymer pairs, while the polymer–polymer interaction is taken to be ideal. This leads to the following pair potentials:

$$u_{cc}(r) = \begin{cases} \infty & r < \sigma_c \\ 0 & \text{otherwise,} \end{cases} \tag{1a}$$

$$u_{cp}(r) = \begin{cases} \infty & r < (\sigma_c + \sigma_p)/2 \\ 0 & \text{otherwise,} \end{cases} \tag{1b}$$

$$u_{pp}(r) = 0 \tag{1c}$$

with r the center-to-center distance between two particles. As bulk thermodynamic parameters, we use the packing fractions $\eta_i = \pi\sigma_i^3 N_i/(6V)$, with V the system volume and N_i the number of particles of species $i = (c, p)$. As an alternative to η_p, we also introduce the polymer reservoir packing fraction η_p^r. For the present case of ideal polymers, one simply has $\eta_p^r = \pi\sigma_p^3 z_p/6$, with z_p the polymer fugacity. The colloid-to-polymer size ratio is denoted $q \equiv \sigma_p/\sigma_c$. As is well known, under certain conditions the AO model phase separates into a colloid-rich (polymer poor) and colloid-poor (polymer rich) domain [19]. If one 'identifies' the colloid-rich phase with a liquid, and the colloid-poor phase with a gas, the phase separation can be treated in much the same way as the liquid–gas transition. In particular, as for the liquid–gas transition, it is possible to construct a binodal.

2.2. Binodal representations

The binodal marks the region in the phase diagram where phase separation occurs. It may be represented in several ways. A popular choice is the reservoir representation, commonly used by computer simulation and density functional theory. Here, one fixes the 'fugacity' η_p^r, and records the respective packing fractions $\eta_c(G)$ and $\eta_c(L)$ of the colloids in the gas and liquid phase. Provided η_p^r exceeds its critical value, coexisting phases can thus be identified. The binodal then becomes a curve in the (η_c, η_p^r)-plane, similar to the (density, temperature)-binodal of simple fluids (strictly speaking, η_p^r must be identified with inverse temperature). Unfortunately, η_p^r is not accessible in experiments, nor by integral equation theory. For this reason, colloid–polymer binodals are often shown in system representation. Here, the actual packing fractions, $\eta_c(G)$ and $\eta_p(G)$, of colloids and polymers in the gas phase are plotted as a single point in the (η_c, η_p)-plane, together with the corresponding point for the liquid phase ($\eta_c(L)$ and $\eta_p(L)$). Compared to the binodal in reservoir representation, the binodal in system representation appears somewhat stretched and rotated. Since we plan to compare simulation data to integral equation theory, the system representation will mostly be used in this work. Nevertheless, in order to emphasize certain trends in the simulation data, the reservoir representation will also occasionally be used.

2.3. Introducing quenched disorder

Next, we explain how the AO model may be extended to also include quenched disorder. According to the quenched–annealed mixture approach [5], the idea is to first generate

a matrix. The matrix is simply a configuration of particles whose spatial coordinates have been selected 'following some recipe'. Once the matrix has been generated, the matrix particles are no longer allowed to move, i.e. their positions are frozen (quenched). Next, the fluid of interest, in our case the AO model, is introduced into the matrix, and properties of interest are collected (here: binodal lines and pair correlation functions). Once these properties have been obtained, the procedure is repeated using a different realization of the matrix, eventually culminating in a quenched average over many different matrix realizations. How this quenched average must be obtained in practice is quite a subtle matter. For integral equation theory, details are provided in section 3 and for the computer simulations in section 4. In this section, we simply outline the *recipes* used by us to construct the matrices. As was announced in section 1, two types of matrix disorder are investigated here.

2.3.1. The polymer matrix. The first approach is to use for the matrix an ideal gas configuration of spheres (species M) of diameter $\sigma_{\rm M}$ at packing fraction $\eta_{\rm M}$. In a computer simulation, such a matrix can easily be generated by distributing the matrix particles randomly through the simulation box. Once the matrix has been generated, colloids and polymers are introduced, which interact with each other via the AO potential. In addition, we couple the colloids and the polymers to the matrix via the following pair potentials

$$u_{\rm cM}(r) = \begin{cases} \infty & r < (\sigma_{\rm c} + \sigma_{\rm M})/2 \\ 0 & \text{otherwise,} \end{cases} \tag{2a}$$

$$u_{\rm pM}(r) = 0, \tag{2b}$$

with r the center-to-center distance. In other words, hard sphere interactions are assumed between colloid–matrix pairs, while polymer–matrix pairs do not interact. In principle, such a matrix could be realized experimentally by trapping polymer particles. Therefore, this realization of quenched disorder is termed a 'polymer' matrix. In the remainder of this work, all results reported for the polymer matrix use a colloid-to-polymer size ratio $q = 1.0$, $\sigma_{\rm c} = \sigma_{\rm M}$, and $\eta_{\rm M} = 0.05$. Note that polymer matrices are also considered theoretically in [12].

2.3.2. The colloid matrix. In the second approach, we use for the matrix an equilibrium hard sphere configuration. From a simulation point of view, such a matrix is slightly more complicated to generate since matrix–matrix pairs may no longer overlap. Here, we let the matrix couple to the colloids and polymers via

$$u_{\rm cM}(r) = \begin{cases} \infty & r < (\sigma_{\rm c} + \sigma_{\rm M})/2 \\ 0 & \text{otherwise,} \end{cases} \tag{3a}$$

$$u_{\rm pM}(r) = \begin{cases} \infty & r < (\sigma_{\rm p} + \sigma_{\rm M})/2 \\ 0 & \text{otherwise,} \end{cases} \tag{3b}$$

with r again the center-to-center distance. In the above, the polymers also experience hard sphere interactions with the matrix. Experimentally, such matrix interactions could be realized by trapping colloidal particles. Hence, we shall refer to this matrix as a 'colloid' matrix. Unless noted otherwise, all results reported for the colloid matrix use a colloid-to-polymer size ratio $q = 0.8$, $\sigma_{\rm c} = \sigma_{\rm M}$, and $\eta_{\rm M} = 0.05$.

3. Integral equation theory

One of the basic ideas underlying the statistical mechanics of quenched–annealed systems exploits the replica method, originally used for spin-glasses [20]. This approach was applied for the first time by Given and Stell, who formulated the counterpart of the Ornstein–Zernike equations for fluids with quenched disorder [7]. This new set of equations, the so-called replica Ornstein–Zernike equations (ROZ), establishes a link between matrix–matrix, matrix–fluid, and fluid–fluid pair correlations. The ROZ set can be solved with the standard closure relations of liquid state theory. As announced in section 1, we explicitly consider three of them, namely the HNC closure

$$B_{ij}^{\rm HNC}(r) = 0, \tag{4}$$

the PY closure

$$B_{ij}^{\rm PY}(r) = \log[1 + \gamma_{ij}(r)] - 1 - \gamma_{ij}(r), \tag{5}$$

and the MS closure

$$B_{ij}^{\rm MS}(r) = [1 - 2\gamma_{ij}(r)]^{1/2} - 1 - \gamma_{ij}(r). \tag{6}$$

In the above, $\gamma_{ij}(r)$ is the indirect correlation function given by $\gamma_{ij}(r) = g_{ij}(r) - c_{ij}(r) - 1$, with $g_{ij}(r)$ and $c_{ij}(r)$ the radial distribution and the direct correlation functions for particles labeled i and j, respectively. The so-called bridge function $B_{ij}(r)$ is related to the other correlations by means of the exact relation

$$g_{ij}(r) = \exp[-\beta u_{ij}(r) + \gamma_{ij}(r) + B_{ij}(r)], \tag{7}$$

where $u_{ij}(r)$ is the AO pair potential for particles labeled i and j. Furthermore, $\beta = 1/k_{\rm B}T$ with $k_{\rm B}$ being the Boltzmann constant and T the absolute temperature. Each of the above closures was solved numerically using a Picard method [21], in which the solution is obtained iteratively by converting the equations to Fourier space, and back again into direct space, until convergence is reached. A standard mixing procedure, in which the 'new' solution uses 90% of the 'old' solution, was implemented to ensure proper convergence. A grid of 1024 points, with a spacing of $0.01\sigma_{\rm M}$, is used in the main part of our calculations (we have checked that no noticeable variation in the structural and thermodynamic quantities is obtained by doubling the number of grid points).

3.1. Thermodynamic quantities

One of the quantities straightforwardly obtained from the correlation functions is the inverse of the isothermal compressibility

$$\left(\beta\frac{\partial P}{\partial \rho}\right)_{T,V,N,\eta_{\rm M}} = \frac{1}{\rho k_{\rm B} T \chi_T} = 1 - \sum_i \frac{\rho_i}{\rho} \sum_j \rho_j \tilde{c}_{ij}(0), \tag{8}$$

where $\tilde{c}_{ij}(0)$ is the Fourier transform of $c_{ij}(r)$ at zero wavevector, ρ_j, $j = (\mathrm{c}, \mathrm{p})$, and ρ are the colloid, polymer, and total densities; V and N are the total volume and the total number of particles, respectively. Another important quantity is the ratio between the (connected) composition–composition structure factor at zero wavevector $S^{\mathrm{C}}_{xx}(0)$ and the corresponding value for an ideal mixture $x(1-x)$ [22]

$$\frac{S^{\mathrm{C}}_{xx}(0)}{x(1-x)} = (1-x)S^{\mathrm{C}}_{\mathrm{pp}}(0) + xS^{\mathrm{C}}_{\mathrm{cc}}(0) - 2(x(1-x))^{1/2}S^{\mathrm{C}}_{\mathrm{cp}}(0), \tag{9}$$

where $x = N_{\mathrm{p}}/(N_{\mathrm{p}} + N_{\mathrm{c}})$ is the polymer composition and $S^{\mathrm{C}}_{\mathrm{pp}}(0)$, $S^{\mathrm{C}}_{\mathrm{cc}}(0)$, $S^{\mathrm{C}}_{\mathrm{cp}}(0)$ are, respectively, the *connected* parts of the polymer–polymer, colloid–colloid and colloid–polymer structure factors at zero wavevector. The peculiarity of connectivity is defined in terms of subsets of Mayer graphs contributing to this structural function (the interested reader may find extended details about it in [7]). In the following text and in the related figures we omit the superscript C (which refers to the feature of connectivity) for not making the notation heavy. High values of $S_{xx}(0)$ signal a trend of phase separation between colloid and polymer species.

The thermodynamic quantity necessary to construct the coexistence curve is the Gibbs free energy at constant pressure, or alternatively the chemical potentials of the two species. The expression of the total pressure for ternary quenched–annealed systems is not straightforwardly obtained by means of the virial equation [23]. Thus, for each composition x (we considered 30 of them between $0.05 < x < 0.95$), we are forced to integrate equation (8) starting from a low density (with total initial packing fraction $\eta_{\mathrm{c}} + \eta_{\mathrm{p}} \leqslant 0.0025$) in order to obtain the pressure. In principle, the availability of a formula relating the chemical potentials to the thermodynamic state point makes it possible to estimate the phase diagram without resorting to thermodynamic integration. However, the necessity of calculating the pressure starting from low density makes fruitless the computational advantage of using such a closed expression for the chemical potentials, for example the one based on the star function [22]. Moreover, the pressure obtained from the compressibility route (see equation (8)) is not expected to be consistent with the one that can be deduced from the Gibbs–Duhem relation because of a lack of thermodynamic and structural consistency of the integral equation theories [23].

This drawback, i.e. the different values achievable for the pressure along the possible thermodynamic routes, also implies that the thermodynamic potentials will vary accordingly. Thus, in order to determine an unambiguous estimate of the phase diagram, one has to take care to use only quantities calculated within the same thermodynamic route. For this reason, we estimate the excess Helmholtz free energy A^{ex} by integrating again the excess part of the pressure starting from low density. Finally, we obtained the excess contribution to the Gibbs free energy via

$$\frac{\beta G^{\mathrm{ex}}}{N} = \frac{\beta A^{\mathrm{ex}}}{N} + \beta P/\rho - 1. \tag{10}$$

The total Gibbs free energy is calculated by adding to the latter quantity the ideal gas part (omitting the kinetic part related to the de Broglie wavelength)

$$\frac{\beta G^{\mathrm{id}}}{N} = x \ln \rho_{\mathrm{p}} + (1-x)\ln \rho_{\mathrm{c}}. \tag{11}$$

The Gibbs free energy was interpolated for composition with cubic splines, and these fits were used to determine the Gibbs free energy at constant pressure.

3.2. Phase coexistence

The coexistence curve was obtained by applying the construction of the common tangent to the Gibbs free energy at constant pressure. By numerical inspection we found that the Gibbs free energy plotted as a function of the composition at constant pressure can be interpolated by a fourth-order polynomial:

$$\frac{\beta G}{N} = \Omega_4 x^4 + \Omega_3 x^3 + \Omega_2 x^2 + \Omega_1 x + \Omega_0, \tag{12}$$

where Ω_i are the corresponding expansion coefficients. For pressures greater than the critical one, the Gibbs free energy turns out to be sampled just on a limited number of state points. This drawback is due to the loss of numerical stability of our algorithm in the proximity of the unmixing spinodal. As explained in [24], the severity of this problem may be estimated from the discriminant Δ of the second-order equation (the second derivative of the polynomial fit of the Gibbs free energy):

$$\Delta = 9\Omega_3^2 - 24\Omega_2\Omega_4. \tag{13}$$

The mixture phase separates into two different equilibrium compositions, whenever Δ becomes greater than zero. In order to check the consistency of our procedure, we monitored Δ as a function of the total pressure, from negative values (at which the Gibbs free energy is fully sampled on a grid of 30 points because there is no phase coexistence), up to positive values. For pressures where Δ varies without manifest discontinuities, the coexistence concentrations can be estimated reliably. In contrast, jumps in the discriminant indicate that the Gibbs free energy is poorly sampled, in which case the coexistence concentrations cannot be reliably obtained. In the upper panel of figure 1, we plot Δ versus the reduced pressure $P^\star = P\sigma_{\mathrm{M}}^3/k_{\mathrm{B}}T$; the lower panel shows the number of (composition) points x where the Gibbs free energy could be obtained, as a function of the pressure. From figure 1, the progressive lack of accurate data at high pressures becomes clear.

In the upper panel of figure 2 we show the Gibbs free energy G for a subcritical pressure $P^* = 0.5$, as well as for a supercritical pressure $P^* = 1.66$. In the lower panel of figure 2 we show the ratio between $S_{xx}(0)$ and the corresponding value for an ideal mixture, for the same two state points as used in the upper panel. Note that this ratio provides a measure of how closely the numerical procedure allows one to approach the spinodal. Phase coexistence properties are readily obtained from the first derivative G' of the free energy with respect to composition (see figure 3). We note that the mixture exhibits a low consolution critical point, thus we observe phase separation at pressures higher

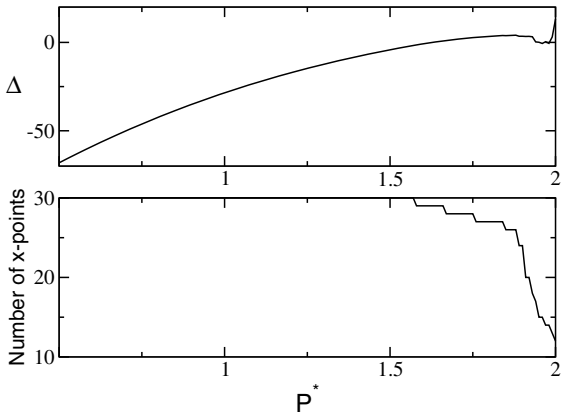

Figure 1. Plots illustrating for which reduced pressures $P^\star = P\sigma_M^3/k_BT$ the coexistence concentrations can be obtained reliably using our method. The data in these plots were obtained for the AO model confined to the polymer matrix. Upper panel: the discriminant Δ of the second derivative of the Gibbs free energy (see text for details) versus $P^\star$. At high pressures, jumps in Δ begin to show-up, in which case our numerical procedure breaks down, and coexistence concentrations can no longer be obtained reliably. Lower panel: number of x points that could be used in the fourth-polynomial fit to the Gibbs free energy, as a function of $P^\star$. At high pressures, x decreases significantly, indicating that coexistence concentrations can no longer be obtained reliably.

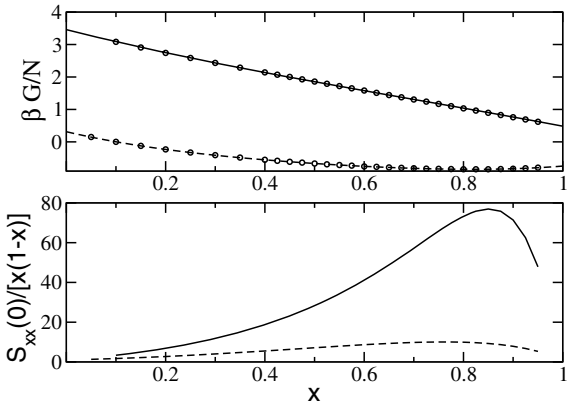

Figure 2. Free energy and structural data for the AO model confined to the polymer matrix. Upper panel: Gibbs free energy G as a function of the polymer composition x at reduced pressure $P^* = 0.5$ (upper curve) and $P^* = 1.66$ (lower curve). The open circles were obtained using the MS closure. The full resp. broken line shows the result of a fourth-order polynomial fit. Lower panel: composition–composition structure factor as a function of the polymer composition for $P^* = 0.5$ (lower curve) and $P^* = 1.66$ (upper curve).

than the critical one. For such pressures, G' exhibits van der Waals-like loops (see the inset of figure 3). In these cases, it is trivial to obtain the binodal compositions (using the Maxwell construction) as well as the spinodal compositions (the relative maximum and minimum of G'). As an illustration, we have calculated G' for a number of pressures P^*, and constructed the binodal and spinodal in figure 4.

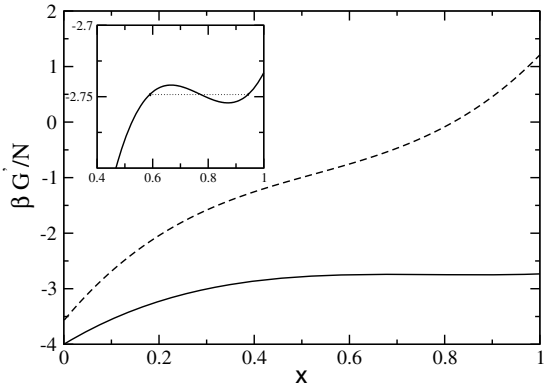

Figure 3. First derivative of the Gibbs free energy G' with respect to composition versus composition x for the AO model confined to a polymer matrix. The full line shows G' at reduced pressure $P^* = 1.66$; the dashed line at $P^* = 0.5$. The inset shows a magnification near the van der Waals loop for $P^* = 1.66$, in order to illustrate the Maxwell construction.

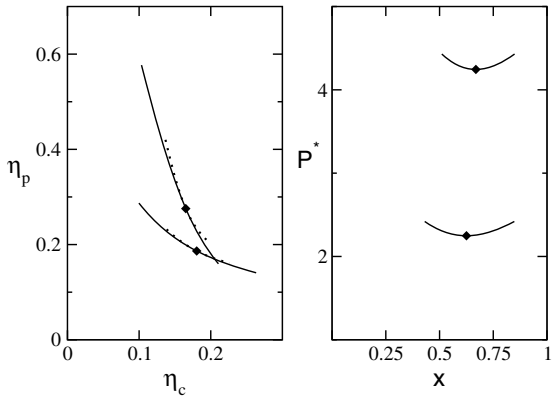

Figure 4. Phase coexistence data of the AO model confined to a *colloid* matrix and using the PY closure relation. The left panel shows the binodal (full lines) and spinodal (dotted lines) in system representation, i.e. using the (η_c, η_p)-plane. The right panel shows the phase diagram in pressure–composition representation (binodals only). In both panels, data for two different colloid-to-polymer size ratios are shown, namely $q = 0.8$ (lower data) and $q = 1.0$ (upper data); diamonds indicate critical points.

4. Computer simulations

4.1. Grand canonical ensemble

Computer simulations of fluids with quenched disorder present a number of complications. In constant pressure and Gibbs ensemble simulations, for example, the volume of the system is a fluctuating quantity. Typically, volume changes are realized via a rescaling of the simulation box. In the presence of a matrix, however, such rescaling operations inevitably alter the matrix, and are therefore not permitted. Consequently, constant pressure and Gibbs ensemble simulations involving quenched disorder require special dedicated algorithms [25, 26]. In this paper, we circumvent the problem by using a grand canonical (GC) ensemble. In the GC ensemble, volume is constant, and so rescaling operations are not needed. Indeed, previous simulations of fluids with quenched disorder have already

exploited the advantages of the GC ensemble [8, 10, 11, 14]. The GC ensemble is moreover powerful because it provides easy access to phase coexistence properties, both in the vicinity of the critical point and away from it. The reason is that, in the GC ensemble, the number of particles fluctuates. This makes it possible to measure the distribution $P(N_c)$, defined as the probability to observe a system with N_c colloids in it. Then, phase coexistence properties can be accurately obtained from the positions of the peaks in $P(N_c)$ [27].

4.2. Establishing coexistence without quenched disorder

In GC simulations of the AO model without quenched disorder, the appropriate control parameters are the fugacities z_c and z_p, of colloid and polymers, respectively (following convention, we use η_p^r instead of z_p). For η_p^r above its critical value, $P(N_c)$ becomes double-peaked (bimodal), provided z_c is tuned to its coexistence value. Away from the critical point, the coexistence z_c can be obtained via the 'equal-area' rule [28, 29]; closer to the critical point, where finite-size effects are important, different criteria can be used [30]. Typical distributions $P(N_c)$ for the AO model (without quenched disorder) have been reported extensively before [27, 31, 32]. From the bimodal form of $P(N_c)$, phase coexistence properties are readily obtained: the peak at low (high) N_c yields the density of the colloidal gas (liquid) phase. We remind the reader that, close to the critical point, such a procedure should always be accompanied with a finite-size scaling analysis.

4.3. Establishing coexistence with quenched disorder

It is possible to extend the above GC approach to the case of an AO model with quenched disorder. Here, the sought-for quantity is the free energy distribution $W(N_c)$, which must be obtained by performing an average over many different realizations of the quenched disorder. $W(N_c)$ can be constructed recursively from the free energy differences $[\Delta F(N_c - 1, N_c)]_{qd}$. For a single realization of quenched disorder, $\Delta F(N_c - 1, N_c)$ is the free energy difference between the states with N_c and $N_c - 1$ colloids; $[.]_{qd}$ represents an average over quenched disorder realizations. The distribution $W(N_c)$ is constructed recursively using

$$\begin{aligned} W(0) &\equiv 0, \\ W(1) &= W(0) + [\Delta F(0, 1)]_{qd}, \\ W(N_c) &= W(N_c - 1) + [\Delta F(N_c - 1, N_c)]_{qd}. \end{aligned} \tag{14}$$

Once $W(N_c)$ is known, the probability distribution in the number of colloids becomes $P(N_c) \propto \exp(-W(N_c)/k_B T)$. Provided η_p^r exceeds its critical value, and z_c assumes its coexistence value, $P(N_c)$ becomes bimodal, and coexistence properties can be obtained in much the same way as before.

4.4. Implementation details

In this work, the GC simulations are performed using a cluster move, whereby colloids and polymers are explicitly included [27, 32]. We use cubic simulation boxes of size $L \times L \times L$ with periodic boundary conditions. At the start of each simulation, a quenched matrix is generated, which, in this work, is either of the 'polymer' or the 'colloid' type. Next, for some η_p^r of interest, the free energy differences $\Delta F(N_c - 1, N_c)$ are obtained using a biased sampling scheme called *successive umbrella sampling* [33]. The idea of this scheme is to divide the simulation into windows. In the first window, N_c is allowed to fluctuate between 0 and 1; in the second, between 1 and 2, and so forth. The number of polymers is allowed to fluctuate freely in each window. The simulation in the first window yields the free energy difference $\Delta F(0, 1)$, essentially by counting how often the states with $N_c = 0$ and $N_c = 1$ were visited [33]. The remaining free energy differences follow from higher windows. This procedure is repeated for many different matrix realizations, typically 100–250, and the free energy differences $\Delta F(N_c - 1, N_c)$ are averaged to obtain $[\Delta F(N_c - 1, N_c)]_{qd}$. These are eventually substituted into equation (14) to obtain the free energy distribution $W(N_c)$. In our simulations, we typically set the colloid fugacity z_c to unity; the coexistence value is obtained afterward using histogram extrapolation [34–36]. In addition, we also store polymer histograms in order to facilitate extrapolations in η_p^r. Obviously, since our GC simulations retain colloid and polymer coordinates explicitly, we have full access to the structural properties at all times. In this work, we calculate the pair correlation functions, which are obtained using a standard method [37], and compared to integral equation theory in section 5.

4.5. Finite-size effects

Again, we emphasize the presence of finite-size effects close to the critical point. For the AO model with quenched disorder, these turn out to be rather peculiar. The point is illustrated in figure 5, which shows the phase diagram in reservoir representation for both the colloid and the polymer matrix. Plotted are binodal curves for several system sizes L. Also shown in figure 5 are the critical points of the $L \to \infty$ systems (squares). The latter were obtained using finite-size scaling. The critical value of η_p^r was extracted from the Binder cumulant [14, 40]. The critical value of η_c (and similarly η_p) was obtained by linearly extrapolating $\eta_c^*(L)$ in the variable $1/L$. Here, $\eta_c^*(L)$ is the value of η_c obtained in a finite system of size L at the critical value of η_p^r. Typically, one expects finite-size effects to vanish away from the critical point. Figure 5 seems to confirm this, but the effect is rather asymmetric. For example, in the colloid matrix, finite-size effects quickly vanish in the liquid branch of the binodal, but remain strong in the gas branch. Interestingly, for the polymer matrix, the trend is reversed.

Also shown in figure 5 are the critical points of the corresponding *bulk* systems without quenched disorder. Compared to these, both the polymer and the colloid matrix shift the critical point to higher η_p^r. This finding is in agreement with the theoretical results of [12], in which colloid and polymer matrices are also treated explicitly. In addition, our data reveal that the corresponding shift in η_c is qualitatively

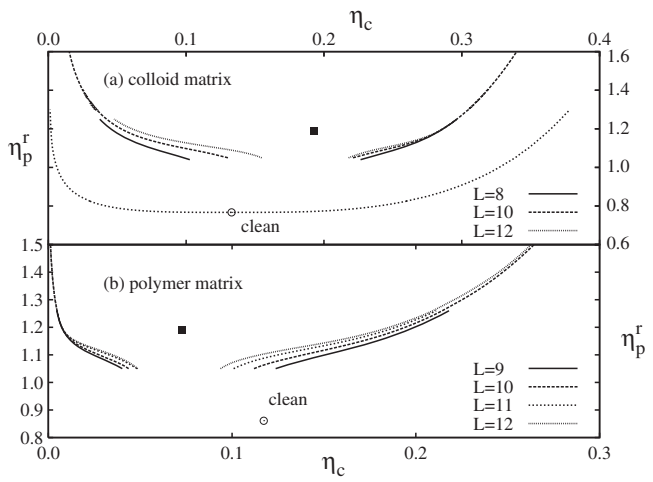

Figure 5. Binodals of the AO model in reservoir representation obtained via GC simulations. Shown is the binodal inside the colloid matrix (a), and the polymer matrix (b), for various system sizes L as indicated. The squares mark the critical points in the thermodynamic limit $L \to \infty$. For comparison, data from the corresponding *clean* systems, i.e. *without* quenched disorder, have also been included. In (a), the binodal of the clean AO model with $q = 0.8$ is shown, where the open circle marks the critical point (data taken from [38]). The open circle in (b) marks the critical point of the clean AO model with $q = 1$, taken from [39].

affected by the type of matrix: for the colloid (polymer) matrix, η_c increases (decreases) compared to its *bulk* value. The results of [12] do not reveal this trend: for both types of matrix, a decrease in η_c is predicted.

5. Results

5.1. Structural properties in the polymer matrix model

We begin the comparison between theory and simulation by considering the polymer matrix model. To this end, we calculated the radial distribution functions (RDFs) of the AO model inside the polymer matrix at two distinct state points.

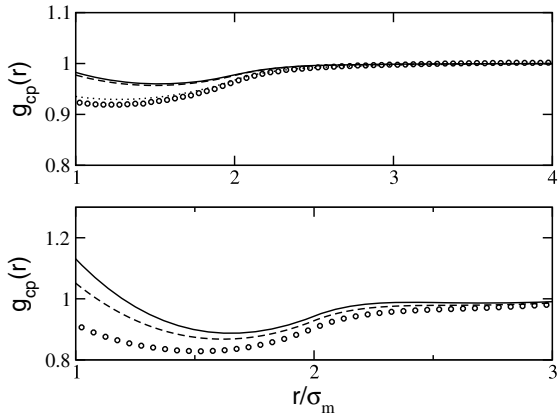

Figure 7. Cross correlations of the AO model inside a polymer matrix. The upper panel shows the colloid–polymer RDF obtained at $\eta_c = 0.025$ and $\eta_p = 0.5$; the lower panel at $\eta_c = 0.15$ and $\eta_p = 0.2$. In both panels, the full lines were obtained using the PY closure, and the dashed lines with the MS closure; circles denote simulation results. Also shown in the upper panel is the HNC result (dotted line). In the lower panel, the HNC result is absent, since no convergent solution could be obtained here.

The first state point is at a low colloid and high polymer packing fraction, namely $\eta_c = 0.025$ and $\eta_p = 0.5$. In figure 6, we show the colloid–colloid and polymer–polymer RDFs for this state point, as well as the correlations with the matrix. Regarding the colloid–colloid RDF, we observe that HNC yields the best agreement with the simulation, while PY and MS evidently underestimate the colloid–colloid RDF at small distances. The same trend also shows up in the polymer–polymer RDF. Here, HNC is almost 'on top' of the simulation result, while PY and MS slightly underestimate it. We also observe that the colloid–matrix and polymer–matrix correlations are almost insensitive to the chosen closure, and in good agreement with the simulation result. The cross colloid–polymer correlations for the selected state point are shown in the upper panel of figure 7. Again, we see good agreement between HNC and simulation, while the PY and MS closures now overestimate the simulation result (at small distances).

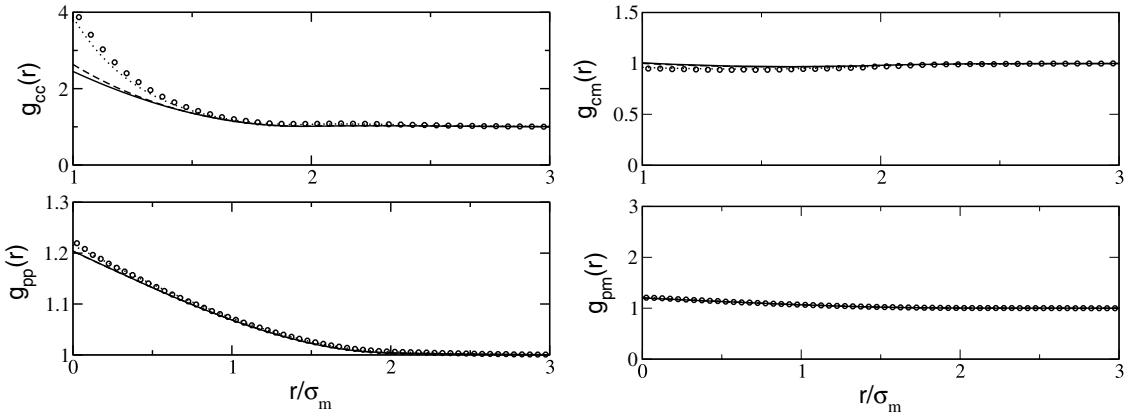

Figure 6. Pair correlation functions of the AO model inside a polymer matrix, obtained at a state point with $\eta_c = 0.025$ and $\eta_p = 0.5$. Shown is the colloid–colloid RDF (upper left), the polymer–polymer RDF (lower left), the colloid–matrix RDF (upper right), and the polymer–matrix RDF (lower right). The full lines are the correlations obtained using the PY closure, dashed lines with the MS closure, and the dotted lines with the HNC closure. The circles denote simulation results.

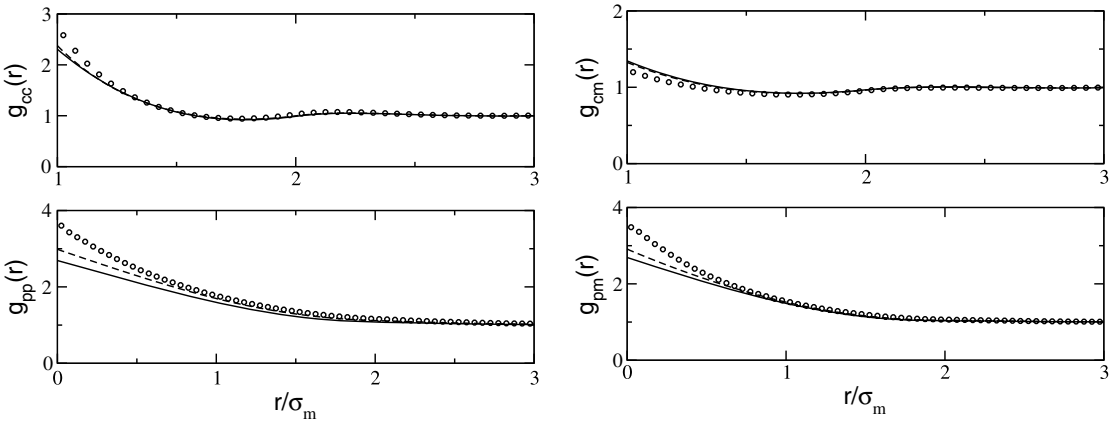

Figure 8. Pair correlation functions of the AO model inside a polymer matrix, obtained at a state point with $\eta_c = 0.15$ and $\eta_p = 0.2$. Shown is the colloid–colloid RDF (upper left), the polymer–polymer RDF (lower left), the colloid–matrix RDF (upper right), and the polymer–matrix RDF (lower right). The full lines are the correlations obtained using the PY closure, dashed lines with the MS closure. The circles denote simulation results. Due to numerical instabilities, no HNC results could be obtained at this state point.

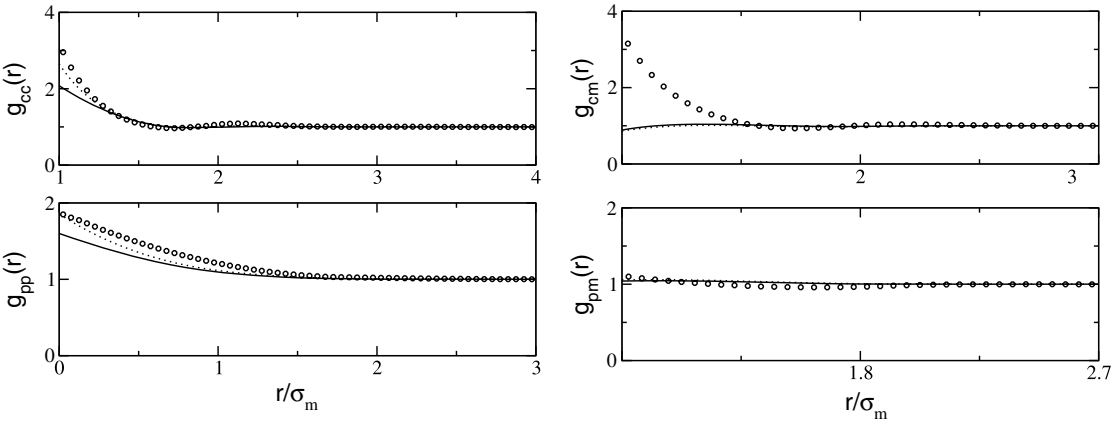

Figure 9. Pair correlation functions of the AO model inside a colloid matrix, obtained at a state point with $\eta_c = 0.05$ and $\eta_p = 0.3$. Shown is the colloid–colloid RDF (upper left), the polymer–polymer RDF (lower left), the colloid–matrix RDF (upper right), and the polymer–matrix RDF (lower right). The full lines are the correlations obtained using the PY closure, the dotted lines with the HNC closure; circles denote simulation results. Due to numerical instabilities, no MS results could be provided for this state point.

The overall good performance of the HNC closure is rather surprising, since this closure is typically considered not to be very precise for short-ranged potentials. Our findings suggest that the shortcomings of the HNC closure are less severe in the case of fluids with quenched disorder, at least for the state point considered here.

Next, we consider a state point at higher colloid, and lower polymer packing fraction, namely $\eta_c = 0.15$ and $\eta_p = 0.2$. Here, we encountered severe numerical difficulties using the HNC closure, while results could still be obtained with PY and MS. Consequently, no results for HNC are reported for this state point. We believe that the numerical difficulties arise from the fact that this state point is rather close to the binodal (see the left phase diagram of figure 12). Our analysis thus suggests that, for such state points, PY and MS are better suited. In figure 8, we show the colloid–colloid and polymer–polymer RDFs, as well as the correlations with the matrix. Regarding the colloid–colloid correlations, PY and MS yield nearly identical results, which agree well with the simulation result except at small distances. In contrast, regarding the polymer–polymer RDF, the PY and MS closures start to deviate from each other at small distances, with MS being closest to the simulation result. This trend is also present in the correlations with the matrix. For the colloid–matrix correlations, PY and MS yield similar results, while for the polymer–matrix correlations, MS clearly gives the best agreement with the simulation. The colloid–polymer cross correlations are also best described by the MS closure (see the lower panel of figure 7). Hence, when describing state points close to the binodal, MS appears to be the most accurate.

5.2. Structural properties in the colloid matrix model

We now consider the AO model inside the colloid matrix model. Again, the RDFs were collected at two state points, the first one being at $\eta_c = 0.05$ and $\eta_p = 0.3$. In figure 9, we show the corresponding colloid–colloid and polymer–polymer RDFs, as well as the correlations with the matrix. At this state

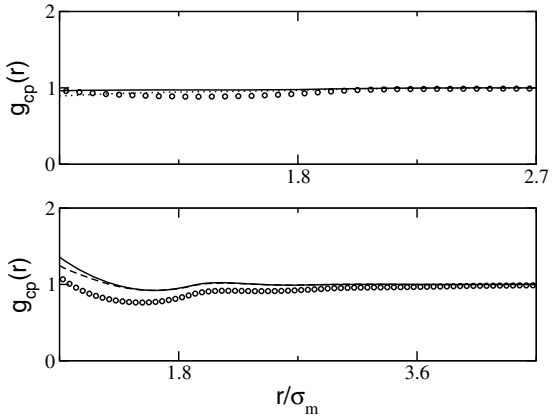

Figure 10. Cross correlations of the AO model inside a colloid matrix. In both panels, the circles denote simulation results. The upper panel shows the colloid–polymer RDF obtained at $\eta_c = 0.05$ and $\eta_p = 0.3$. At this state point, no MS result could be obtained, and so we only report PY (solid line) and HNC (dotted line). The lower panel shows the colloid–polymer RDF at $\eta_c = 0.225$ and $\eta_p = 0.1$. At this state point, the HNC closure failed to converge, and so we only report the PY result (solid line) and the MS result (dashed line).

point, we could not achieve a convergent solution using the MS closure, leaving only the HNC and PY results. Regarding the colloid–colloid and polymer–polymer correlations, HNC and PY yield similar results, with HNC being slightly closer to the simulation result. However, both closures evidently fail to predict the colloid–matrix correlations at short distances. In this regime, the simulated colloid–matrix RDF rises quite steeply, while the HNC and PY curves remain essentially flat. Regarding the polymer–matrix correlations, the agreement of HNC and PY with the simulation is better (although closer inspection does reveal some curvature in the simulation result, not reproduced by the theories). The colloid–polymer cross correlations for the selected state point are shown in the upper panel of figure 10. Here, we observe overall good agreement between both closures and the simulation result, HNC being slightly superior.

For the second state point, we choose $\eta_c = 0.225$ and $\eta_p = 0.1$. In figure 11, we show the corresponding colloid–colloid and polymer–polymer RDFs, as well as the correlations with the matrix. At this state point, we could not achieve a convergent solution using the HNC closure, leaving only the PY and MS results. As figure 11 shows, with the exception of the polymer–polymer correlations, both closures yield similar results. Regarding the colloid–colloid correlations, the agreement with the simulation is very good. For the remaining correlations, at short distances, pronounced deviations from the simulations arise. Regarding the polymer–polymer correlations, PY and MS yield different results, with MS being closest to the simulation result. Interestingly, this trend also appeared in the polymer matrix model (see the lower left frame of figure 8). The colloid–polymer cross correlations are shown in the lower frame of figure 10. Again, PY and MS deviate slightly from each other at short distances, with MS showing the best agreement with the simulation.

5.3. Binodal

Finally, we consider the binodal curves. Due to the difficulty of reaching critical pressures, we were unable to construct the binodal using the HNC closure. We only succeeded in this accomplishment using the PY and MS closures. In the left frame of figure 12, we show the PY and MS binodals, as well as the simulation result, for the polymer matrix model. Also shown is the density functional theory (DFT) result of [12]. We observe that all the theoretical binodals underestimate the simulation result considerably. The simulated critical point is at $\eta_c = 0.073$ and $\eta_p = 0.807$. The theoretical estimates read as $\eta_c = 0.121$ and $\eta_p = 0.253$ for the PY closure; $\eta_c = 0.109$ and $\eta_p = 0.304$ for the MS closure; the DFT critical point is at $\eta_c = 0.097$ and $\eta_p = 0.278$. The critical colloid packing fraction is thus best captured by the DFT, while the critical polymer packing fraction is captured slightly better by the PY and MS closures. The problem of convergence of the closures was even more severe in the colloid matrix model (see the right frame of figure 12). Here, the binodal could only be obtained using the PY closure. However, the theoretical solution is

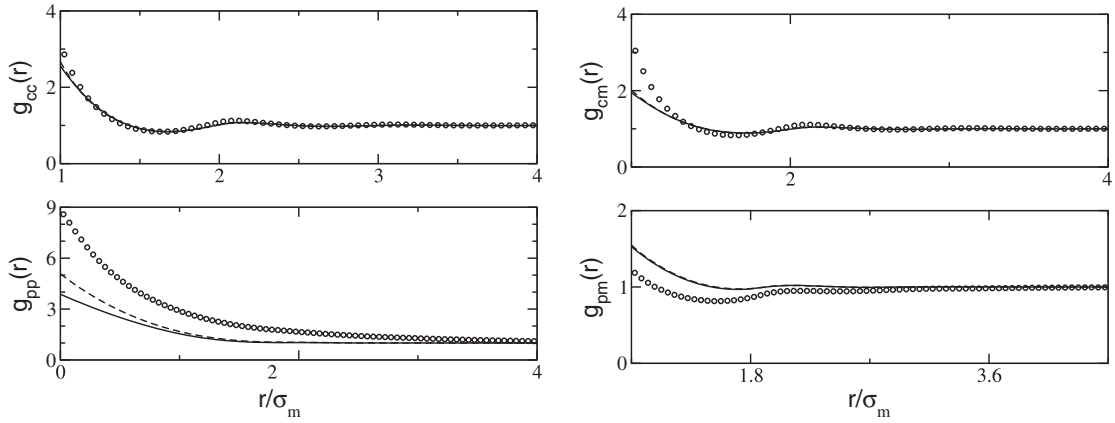

Figure 11. Pair correlation functions of the AO model inside a colloid matrix, obtained at a state point with $\eta_c = 0.225$ and $\eta_p = 0.1$. Shown is the colloid–colloid RDF (upper left), the polymer–polymer RDF (lower left), the colloid–matrix RDF (upper right), and the polymer–matrix RDF (lower right). The full lines are the correlations obtained using the PY closure, the dashed lines with the MS closure; circles denote simulation results. Due to numerical instabilities, no HNC results could be provided for this state point.

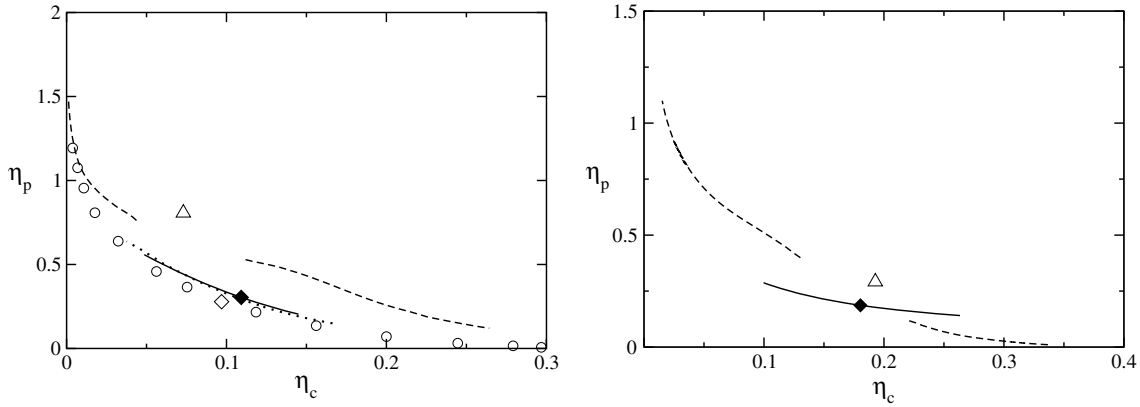

Figure 12. Binodal curves in system representation of the AO model in the presence of quenched disorder, as obtained using computer simulation and various theoretical approaches. In both frames, the dashed lines show the binodal obtained in the simulations of the present work, where the open triangle is the corresponding simulation estimate of the critical point in the thermodynamic limit. The left frame shows results for the polymer matrix, the right frame for the colloid matrix. For the polymer matrix, the binodal could only be obtained using the MS closure (solid line) and PY (dotted line). For completeness, the DFT result of [12] is also shown (open circles). The critical points for the DFT and the MS curves are depicted with the open and full diamonds, respectively. The right frame shows the binodal for the colloid matrix model. Here, only the PY closure converged (solid line), with the black diamond marking the location of the critical point.

clearly not very accurate, since it does not even capture the slope of the simulated binodal. For the colloid matrix model, the critical point obtained in the simulations is at $\eta_c = 0.192$ and $\eta_p = 0.292$, to be compared to the PY values $\eta_c = 0.180$ and $\eta_p = 0.186$.

6. Conclusions

In summary, we have studied the structural properties and the unmixing transition in the Asakura–Oosawa model of colloid–polymer mixtures in the presence of different types of quenched disorder. Our theoretical approach was based on the replica Ornstein–Zernike equations, using the HNC, PY and MS integral equation closures. Our simulation approach utilized the grand canonical Monte Carlo method. We found that all three closures can reasonably predict the structural properties of the Asakura–Oosawa model in the presence of quenched polymer disorder, HNC being the most reliable. However, HNC fails to capture the phase coexistence properties and better results are achieved within the PY and MS closures.

When quenched colloid disorder is considered, the performance of the three closures becomes unreliable, and they do not even qualitatively capture the shape of the unmixing binodal. This inadequacy prompts the adoption of more refined approaches based on self-consistency strategies, such as those hinging upon thermodynamic or structural constraints [16]. Our simulation results may serve as benchmark data for future tests of such more sophisticated theories.

For the future, we foresee three conceivable routes to advance our theoretical understanding of fluids with quenched disorder. First of all, it would be interesting to develop a liquid-integral equation theory which correctly predicts the phase behavior close to the critical point (which should resemble that of the random-field Ising model [14]). This may be achieved via a generalization of the hierarchical reference theory [41] to fluids with quenched disorder. Second, different particle shapes other than spheres should be considered, such as rod-like colloidal particles and solutes [42]. In soft-matter systems, quenched disorder involving non-spherical particles is already a reality [43]. Finally, it would be challenging to extend the static density functional theory for the Asakura–Oosawa model [44–48] toward both dynamical and non-equilibrium situations [49]. This has already been performed in the bulk [50–54], but the application to a porous medium is still elusive.

Acknowledgments

This work was supported by the *Deutsche Forschungsgemeinschaft* under the SFB-TR6 (project section D3) and by the Marie Curie European Network MRTN-CT-2003-504712.

References

[1] Sahimi M 1993 *Rev. Mod. Phys.* **65** 1393–534
[2] de Gennes P G 1984 *J. Phys. Chem.* **88** 6469
[3] Wong A P Y and Chan M H W 1990 *Phys. Rev. Lett.* **65** 2567
[4] Wong A P Y, Kim S B, Goldburg W I and Chan M H W 1993 *Phys. Rev. Lett.* **70** 954
[5] Madden W G and Glandt E D 1988 *J. Stat. Phys.* **51** 537
[6] Madden W G 1992 *J. Chem. Phys.* **96** 5422
[7] Given J A and Stell G 1994 *Physica* A **209** 495
[8] Álvarez M, Levesque D and Weis J J 1999 *Phys. Rev.* E **60** 5495
[9] Sarkisov L and Monson P A 2000 *Phys. Rev.* E **61** 7231
[10] De Grandis V, Gallo P and Rovere M 2004 *Phys. Rev.* E **70** 061505
[11] Schöll-Paschinger E, Levesque D, Weis J J and Kahl G 2001 *Phys. Rev.* E **64** 011502
[12] Schmidt M, Schöll-Paschinger E, Köfinger J and Kahl G 2002 *J. Phys.: Condens. Matter* **14** 12099
[13] Kierlik E, Rosinberg M L, Tarjus G and Monson P A 1996 *J. Phys.: Condens. Matter* **8** 9621

[14] Vink R L C, Binder K and Löwen H 2006 *Phys. Rev. Lett.* **97** 230603
[15] Schöll-Paschinger E and Kahl G 2000 *Phys. Rev.* E **61** 5330
[16] Caccamo C 1996 *Phys. Rep.* **274** 1
[17] Asakura S and Oosawa F 1954 *J. Chem. Phys.* **22** 1255
[18] Vrij A 1976 *Pure Appl. Chem.* **48** 471
[19] Lekkerkerker H, Poon W, Pusey P, Stroobants A and Warren P 1992 *Europhys. Lett.* **20** 559
[20] Given J A 1992 *Phys. Rev.* A **45** 816
[21] Hansen J P and McDonald I R 1976 *Theory of Simple Liquids* (London: Academic)
[22] Duda Y, Pizio O and Sokolowsi S 2004 *J. Phys. Chem.* B **108** 19442
[23] Pellicane G, Caccamo C, Wilson D and Lee L L 2004 *Phys. Rev.* E **69** 061202
[24] Pellicane G, Saija F, Caccamo C and Giaquinta P 2006 *J. Phys. Chem.* B **110** 4539
[25] Brennan J K and Dong W 2002 *J. Chem. Phys.* **116** 8948
[26] Puibasset J 2005 *J. Chem. Phys.* **122** 134710
[27] Vink R L C and Horbach J 2004 *J. Chem. Phys.* **121** 3253
[28] Binder K and Landau D P 1984 *Phys. Rev.* B **30** 1477
[29] Müller M and Wilding N B 1995 *Phys. Rev.* E **51** 2079
[30] Orkoulas G, Fisher M E and Panagiotopoulos A Z 2001 *Phys. Rev.* E **63** 051507
[31] Vink R L C and Horbach J 2004 *J. Phys.: Condens. Matter* **16** S3807
[32] Vink R L C 2004 *Computer Simulation Studies in Condensed Matter Physics* vol XVII ed D P Landau, S P Lewis and H B Schüttler (Berlin: Springer) p 45
[33] Virnau P and Müller M 2004 *J. Chem. Phys.* **120** 10925
[34] Ferrenberg A M and Swendsen R H 1989 *Phys. Rev. Lett.* **63** 1195
[35] Ferrenberg A M and Swendsen R H 1988 *Phys. Rev. Lett.* **61** 2635
[36] Newman M E J and Barkema G T 1999 *Monte Carlo Methods in Statistical Physics* (Oxford: Clarendon)
[37] Allen M P and Tildesley D J 1989 *Computer Simulation of Liquids* (Oxford: Oxford University Press)
[38] Vink R L C, Binder K and Horbach J 2006 *Phys. Rev.* E **73** 056118
[39] Fortini A, Schmidt M and Dijkstra M 2006 *Phys. Rev.* E **73** 051502
[40] Binder K 1981 *Z. Phys.* B **43** 119
[41] Reatto L and Parola A 1996 *J. Phys.: Condens. Matter* **8** 9221
[42] Sarkisov L and van Tassel P R 2005 *J. Chem. Phys.* **123** 164706
[43] Kluijtmans S G J M, Koenderink G H and Philipse A P 2000 *Phys. Rev.* E **61** 626–36
[44] Schmidt M, Löwen H, Brader J M and Evans R 2000 *Phys. Rev. Lett.* **85** 1934
[45] Brader J M, Evans R, Schmidt M and Löwen H 2002 *J. Phys.: Condens. Matter* **14** L1
[46] Schmidt M, Löwen H, Brader J M and Evans R 2002 *J. Phys.: Condens. Matter* **14** 9353
[47] Wessels P P F, Schmidt M and Löwen H 2004 *J. Phys.: Condens. Matter* **16** L1
[48] Wessels P P F, Schmidt M and Löwen H 2005 *Phys. Rev. Lett.* **94** 078303
[49] Löwen H 2001 *J. Phys.: Condens. Matter* **13** R415
[50] Marconi U M B and Tarazona P 1999 *J. Chem. Phys.* **110** 8032
[51] Marconi U M B and Tarazona P 2000 *J. Phys.: Condens. Matter* **12** A413
[52] Archer A J and Evans R 2004 *J. Chem. Phys.* **121** 4246
[53] Dzubiella J and Likos C N 2003 *J. Phys.: Condens. Matter* **15** L147
[54] Rex M, Wensink H H and Löwen H 2007 *Phys. Rev.* E **76** 021403